PHYSICAL REVIEW MATERIALS **6**, 064404 (2022)

Unusual magnetic and transport properties in $HoMn_6Sn_6$ kagome magnet

Firoza Kabir,[1] Randall Filippone,[2] Gyanendra Dhakal,[1] Y. Lee,[3] Narayan Poudel,[4] Jacob Casey,[2]
Anup Pradhan Sakhya,[1] Sabin Regmi,[1] Robert Smith,[1] Pietro Manfrinetti,[5,6] Liqin Ke,[3]
Krzysztof Gofryk,[4] Madhab Neupane,[1,*] and Arjun K. Pathak[2,†]
[1]*Department of Physics, University of Central Florida, Orlando, Florida 32816, USA*
[2]*Department of Physics, SUNY Buffalo State, Buffalo, New York 14222, USA*
[3]*Ames Laboratory, US Department of Energy, Ames, Iowa 50011, USA*
[4]*Idaho National Laboratory, Idaho Falls ID 83402, USA*
[5]*Department of Chemistry, University of Genova, 16146 Genova, Italy*
[6]*Institute SPIN-CNR, 16152 Genova, Italy*

(Received 2 November 2021; accepted 18 May 2022; published 7 June 2022)

With intricate lattice structures, kagome materials are an excellent platform to study various fascinating topological quantum states. In particular, kagome materials, revealing large responses to external stimuli such as pressure or magnetic field, are subject to special investigation. Here we study the kagome-net $HoMn_6Sn_6$ magnet that undergoes paramagnetic to ferrimagnetic transition (below 376 K) and reveals spin-reorientation transition below 200 K. In this compound, we observe the topological Hall effect and substantial contribution of anomalous Hall effect above 100 K. We unveil the pressure effects on magnetic ordering at a low magnetic field from the pressure tunable magnetization measurement. By utilizing high-resolution angle-resolved photoemission spectroscopy, Dirac-like dispersion at the high-symmetry point K is revealed in the vicinity of the Fermi level, which is well supported by the first-principles calculations. Our investigation will pave the way to understanding the magnetotransport and electronic properties of various rare-earth-based kagome magnets.

DOI: 10.1103/PhysRevMaterials.6.064404

I. INTRODUCTION

Topological nontrivial magnetic materials have attracted tremendous attention, and kagome magnets are one of them, which reveal various interesting electronic states such as Dirac fermions [1,2], intrinsic Chern quantum phases, and spin-liquid phases [3–8]. Among these kagome materials, transition-metal-based kagome magnets [1,2,9–16] have already appeared to be the distinguished candidates for correlated topological states, as they possess both unusual magnetic tunability and large Berry curvature fields. These materials are also predicted to support intrinsic Chern quantum phases [17,18] due to their extraordinary lattice geometry and broken time-reversal symmetry. In addition, a number of nontrivial magnetic phases have been observed in the rare-earth-and-transition-metal-based RMn_6Sn_6 family (R = rare earth) [19–25]. Recently, $TbMn_6Sn_6$, one of the members of this 166 family, has been identified as a Chern magnet where a large anomalous Hall effect (AHE) and the quantized Landau fan diagram featuring spin-polarized Dirac dispersion with a large Chern gap have been observed [7]. In another member of this family, YMn_6Sn_6, a topological Hall effect has been revealed [26–28] and explained by a new chirality mechanism originated from frustrated interplanar exchange interactions and the induced strong magnetic fluctuations. Lately, Gao *et al.* have reported AHE in RMn_6Sn_6 (R = Tb, Dy, Ho) with clean Mn kagome lattice [29]. Dhakal *et al.* have recently studied magnetic, magnetotransport, and angle-resolved spectroscopic measurement of $ErMn_6Sn_6$ [30]. Thus each member of the RMn_6Sn_6 family is catching extensive attention for experimental exploration.

In this article, we explore another member of the RMn_6Sn_6 family, $HoMn_6Sn_6$, which consists of two magnetic sublattices: Ho and Mn. Neutron-diffraction studies and magnetic measurements [31–34] suggested that Mn and Ho sublattices simultaneously transfer from the paramagnetic state to ordered states below a critical temperature of $T_C = 376$ K. With further lowering of temperature, the easy direction of the ordered state starts to reorient from the basal plane toward the c axis below 200 K [32]. The canting angle with respect to [001] is $\sim 49^\circ$ at 100 K and remains constant down to 2 K [32]. The mechanism of the spin-reorientation (SR) transition of $HoMn_6Sn_6$ has been quantitatively investigated in a molecular-field theory [31]. However, detailed magnetic, transport, and angle-resolved spectroscopic measurements along with theoretical investigation of $HoMn_6Sn_6$ have not been reported yet.

Hence we have performed systematic studies of transport and magnetic behaviors (at ambient and applied pressure) of the $HoMn_6Sn_6$ kagome magnet. By utilizing angle-resolved photoemission spectroscopy (ARPES), we have measured the electronic structure of this compound, which has been supported by first-principles calculations. The electrical transport measurement indicates that the compound is metallic and

---

[*] Corresponding author: madhab.neupane@ucf.edu

[†] Corresponding author: pathakak@buffalostate.edu

2475-9953/2022/6(6)/064404(7)

shows a large AHE and topological Hall effect contribution in $HoMn_6Sn_6$ at temperatures close to the SR transition temperature, T_{SR}. Furthermore, we measure the magnetizations with external fields applied along the in- and out-of-plane directions when the temperature decreases from 400 to 2 K. At $T = 2$ K, a well-defined magnetization loop for the field applied along the c axis suggests a strong out-of-plane magnetization component. Thus this compound could be a potential candidate for Chern-gapped topological material, according to the Haldane model [17,18,35–37]. Moreover, magnetization measurements under pressure reveal the pressure effects on magnetic ordering at low magnetic fields and below T_{SR} (200 K). ARPES measurements demonstrate the presence of Dirac-like states at the high-symmetry point K, close to the Fermi level E_F. Our exploration of electronic and magnetic properties of $HoMn_6Sn_6$ will provide an effective way to reveal the magnetotransport behaviors of various rare-earth kagome magnets.

II. METHODS

Single crystals of $HoMn_6Sn_6$ were grown by the Sn flux technique as described in the Supplemental Material (SF.1) [38]. DC magnetization and transport measurements were carried out using the physical property measurement system. Resistivity and Hall resistivity measurements were performed using the conventional four-probe method. The resistivity was measured by applying the current (I) along the ab plane and the field was applied along the c axis. A large residual resistivity ratio, RRR = 68, indicates a high quality of the single crystals used in this study.

DFT calculations are performed using a full-potential linear augmented plane-wave method as implemented in WIEN2k [39]. The generalized gradient approximation of Perdew, Burke, and Ernzerhof [40] is used for the correlation and exchange potentials. To generate the self-consistent potential and charge, we employed $R_{MT}K_{max} = 8.0$ with muffin-tin (MT) radii $R_{MT} = 2.7$, 2.4, and 2.5 a.u. for Ho, Mn, and Sn, respectively. The calculations are performed with 264 k points in the irreducible Brillouin zone (BZ) and iterated until the total energy difference is lower than 0.01 mRy. Spin-orbit coupling (SOC) is included with the second-variational method. Besides using the DFT + U method, we also treated the $4f$ states in an open-core approach to keep the band structures near Fermi level from the influence of the $4f$ states. The primitive cell contains one formula unit (f.u.). We adopt experimental lattice parameters [33] in calculations.

We construct the TB Hamiltonian by using 118 maximally localized Wannier functions [41], 59 for each spin channel, corresponding to d-type orbitals for Ho and Mn atoms, and s- and p-type orbitals for Sn atoms in the unit cell. SOC mixes the spin-up and spin-down states. The resulting real-space Hamiltonians $H(\mathbf{R})$ with a dimension of 118 × 118 accurately represent the band structures within the energy window of interest around E_F.

The electronic structure of $HoMn_6Sn_6$ was measured by ARPES at the SLS SIS-X09LA BL at 20 K with a photon energy of 100 eV and under ultrahigh vacuum conditions (5×10^{-11} Torr). High quality samples were used for the measurements. The crystals were cut into small pieces and mounted on the sample plate with copper posts on top of them. After that the samples were loaded into the chamber, and the chamber was cooled and pumped down for few hours. The samples were cleaved *in situ*. For the synchrotron measurements, the energy resolution was better than 20 meV and the angular resolution was set to be finer than 0.2°. The measurements were carried out for more than 15 h without noticeable decay or damage of the samples.

III. RESULTS

A. Crystal structure and electrical transport measurement

$HoMn_6Sn_6$ crystallizes into a $HfFe_6Ge_6$-type structure (space group is P6/mmm, No. 191), as shown in Fig. 1(a) with Ho at 1(a) (0, 0, 0), Mn at 6(i) (1/2, 0, z ∼ 0.249), and Sn at 2(c) (1/3, 2/3, 0), 2(d) (1/3, 2/3, 1/2), and 2(e) (0, 0, z ∼ 0.34) [42], which is composed of the Ho layer consisting of Sn atoms and Mn kagome nets stacked in the sequence -Mn-Ho-Mn-Mn-Ho-Mn- along the c axis [31]. The Ho and Sn_2 atoms lie in the same plane and Mn-$Sn_1 - Sn_3 - Sn_1$-Mn atoms are stacked along the c axis alternatively. The Mn atoms form two kagome layers and the Sn_2 and Sn_3 atoms form a hexagonal structure. The hexagonal structure formed by Sn_2 atoms can be clearly observed from Fig. 1(b) while viewing along the c axis. The Ho atoms lie at the center of the hexagons formed by the Sn_2 atoms, clearly visible from Fig. 1(b). Sn_3 is below the Sn_2 layers; hence the Sn_3 layer is invisible from this top view in Fig. 1(b). The Ho atom lies at the center of the hexagons surrounded by the Sn_2 atoms. On the other hand, being positioned below or above the Ho atoms, the Sn_1 atoms could not be detected from this top view of Fig. 1(b). Figure 1(c) shows the three-dimensional (3D) BZ and its hexagonal-shaped projection onto the (001) plane.

The temperature-dependent resistivity measured along $H \parallel c$, as plotted in Fig. 1(d), shows the metallic behavior of the sample over the measured temperature range of 1.8 to 400 K. The SR transition at ∼200 K is not visible in $\rho(T)$ in Fig. 1(d). However, the ferromagnetic transition of Mn sublattice at $T_C = 373$ K has been observed, clearly seen in $dR/dT(T)$ [see the inset at the right corner of the Fig. 1(d)]. The inset at the upper left corner shows an anomaly at low-temperature ($T = 3$ K) resistivity at zero magnetic field. The origin of the anomaly is unclear, but it can be suppressed by the application of a magnetic field as weak as 0.05 T. Figure 1(e) presents the magnetoresistance [$MR(H)$] of $HoMn_6Sn_6$, showing a relatively large value of MR=70% at $\Delta H = 9$ T. Interestingly, the MR at 2 K shows a linear behavior as a function of the magnetic field, suggesting the materials hosting Dirac-like states. Figure 1(f) presents the magnetic-field dependence of the Hall resistivity in $HoMn_6Sn_6$. As can be seen from the figure, there is a strong contribution of AHE for temperatures above 100 K, and the overall behavior of Hall resistivity resembles the $M(H)$ data shown in Fig. 2(d).

In topological magnetic materials, the total Hall resistivity (ρ_H) can be expressed as

$$\rho_H = \rho^A + \rho^N + \rho^T, \tag{1}$$

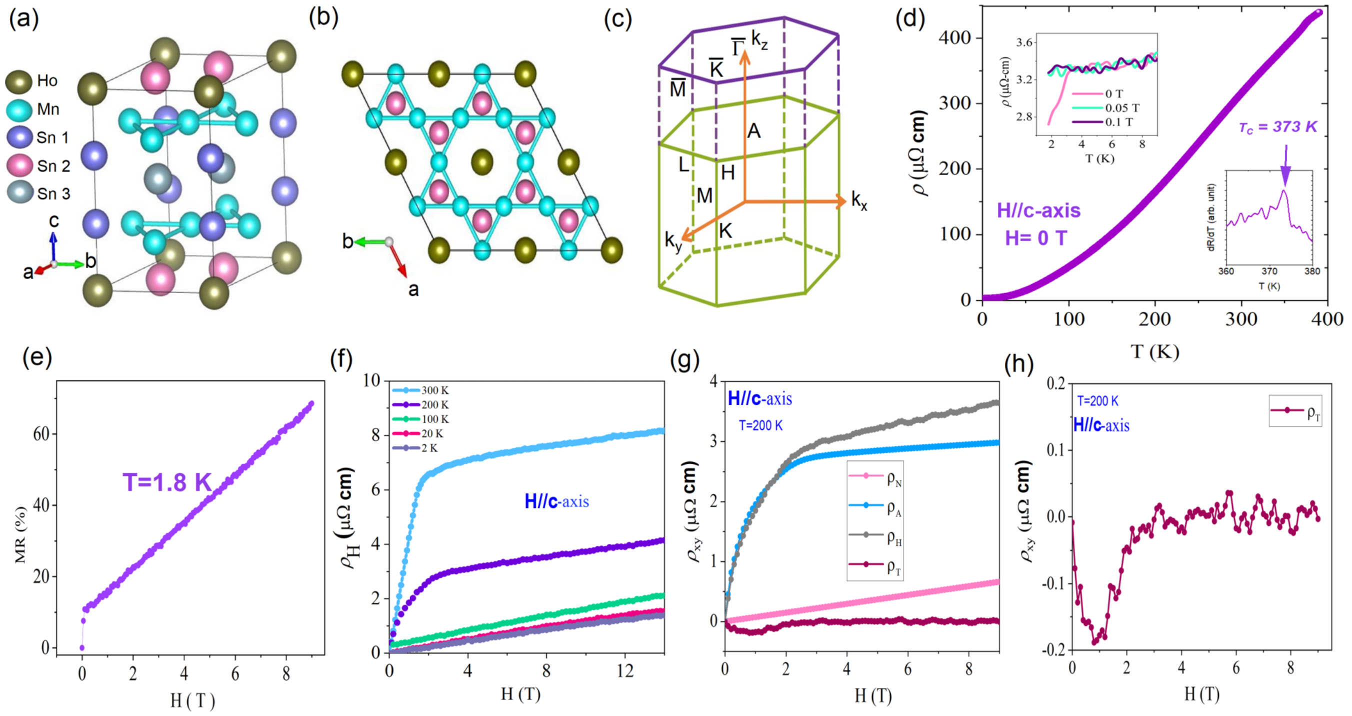

FIG. 1. Crystal structure and sample characterization of $HoMn_6Sn_6$: (a) Crystal structure of $HoMn_6Sn_6$. (b) Top view of the crystal structure of $HoMn_6Sn_6$ forming the kagome lattice. (c) Three-dimensional (3D) bulk BZ of the crystal with its projection on the [001] surface. High-symmetry points are marked on the plot. (d) Temperature variation of the electrical resistivity of $HoMn_6Sn_6$ in zero external magnetic field. The upper inset to the left shows the resistivity at low temperature and magnetic field, while the lower inset to the right indicates the ferrimagnetic transition at $T_C = 373\,\mathrm{K}$. (e) Magnetoresistance versus magnetic field measured at $T = 1.8\,\mathrm{K}$. (f) Hall resistivity of $HoMn_6Sn_6$ measured at different temperatures along $H \parallel c$. (g) Magnetic-field dependence of total Hall resistivity together with the three different components, ρ^A, ρ^N, and ρ^T (see text for more details), measured with $H \parallel c$, and at $T = 200$ K. (h) Magnetic-field dependence of topological Hall resistivity along $H \parallel c$ (magnified view).

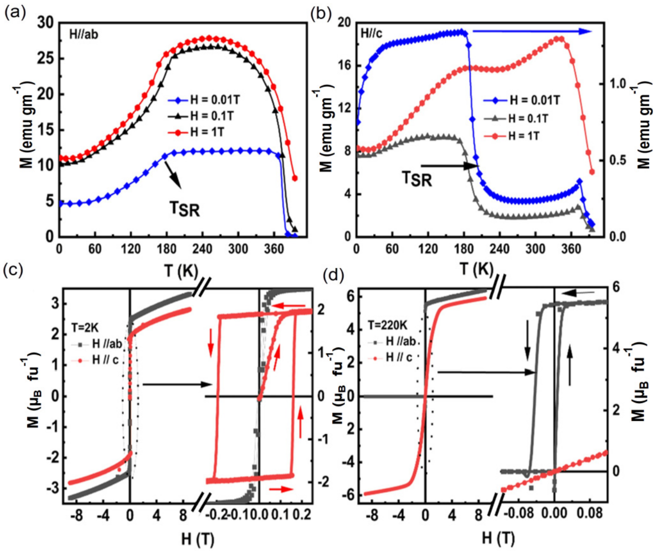

FIG. 2. Magnetic properties of $HoMn_6Sn_6$ single crystals measured along $H \parallel ab$ and $H \parallel c$ (in and out of plane, respectively): Magnetization as a function of temperature, $M(T)$, measured along (a) $H \parallel ab$ and (b) $H \parallel c$, respectively, at various magnetic fields. Magnetization as a function of magnetic field, $M(H)$, measured along $H \parallel ab$ and $H \parallel c$ at (c) $T = 2$ K and (d) 220 K, respectively. Magnetization at low magnetic field of $M(H)$ for both directions are also shown in the right sides of figures (c) and (d), respectively, for the clarity.

where $\rho^A = R_S 4\pi M$ is the anomalous Hall resistivity, $\rho^N(H) = R_0 H$ is the normal Hall resistivity, and ρ^T refers to the topological Hall resistivity. Equation (1) can be rewritten as $\rho_H = R_0 H + R_S 4\pi M$ in the high-field saturation region. We calculate the slope R_0 and intercept $4\pi R_S$ from the linear plot of ρ_H/M versus H/M in the high-magnetic-field region. At that region, the ideal linear behavior of the ρ_H/M versus H/M indicates the anomalous Hall resistivity to be the main component of the total Hall resistance. The R_0 derived for $H \parallel c$ and at $T = 200\,\mathrm{K}$ gives positive ρ^N [see Fig. 1(g)]. We derive the topological Hall resistivity by subtracting the normal and anomalous component of the Hall resistivity from the total Hall resistivity.

As can be clearly seen from the magnified view of the topological Hall resistivity [Fig. 1(h)], the contribution of the topological Hall effect is small compared with anomalous Hall resistivity, but its value is comparable to other topological materials [28,43]. The magnitude of topological Hall resistivity is maximum ($\sim 0.2\,\mu\Omega$-cm) at a relatively low magnetic field of ~1 T, temperature T = 200 K, and decreases with further increase in the field and has negligible effect for H $\geqslant$ 2.2 T. Similar behavior has been reported in the YMn_6Sn_6 kagome magnet in which the topological Hall effect ρ_{xy}^T reaches -$\sim 0.28\,\mu\Omega$-cm at H = 4 T and T = 220 K and decreases with further increase in a magnetic field. The change of the topological Hall effect in YMn_6Sn_6 is ascribed to the magnetic structure at the higher magnetic field [28].

B. Magnetic properties and pressure-induced magnetization

Figures 2(a) and 2(b) show the isofield magnetization $M(T)$ measured with different in- and out-of-plane magnetic fields, exhibiting two distinct transitions for both directions. Figure 2(a) presents the $M(T)$ measured at three representative in-plane magnetic fields: $H = 0.01$, 0.1, and 1 T. At $H = 0.01$ T, the magnetization increases smoothly with temperature until $T \leqslant 190$ K, becomes plateaued between 200 and 360 K, and finally undergoes phase transition at 374 K (obtained from minima of dM/dT). The high-temperature phase transition at $H = 0.01$ T is close to the previously reported ferrimagnetic-to-paramagnetic-transition temperature of $T_C = 376$ K for a polycrystalline sample by Venturini *et al.* [31].

The obtained transition temperature at T = 190 K corresponds to the SR temperature, T_{SR}, which compares well with the previously reported value of $T_{SR} = 200$ K, obtained from neutron diffraction. Interestingly, applying external magnetic fields slightly decreases T_{SR} but significantly increases T_C. The ferrimagnetic-to-paramagnetic transition does not complete until 400 K at $H \geqslant 1$ T, which is also shown in the nonlinear $M(H)$ measured at $T = 390$ K (Supplemental Fig. SF. 2) [38]. It is also noticeable that, along $H \parallel ab$, at $H = 1$ T, the low-temperature ($T \leqslant T_{SR}$) magnetization is larger compared with the measurement along $H \parallel c$, and the magnetization difference decreases at $T \geqslant T_{SR}$. The typical isothermal magnetization for both $H \parallel ab$ and $H \parallel c$ at $T = 2$ and 220 K (below and above the T_{SR}) is shown in Figs. 2(c) and 2(d), respectively. At $T = 20$ K and $H = 9$ T, the magnetic moments are 3.14 and 2.8 μ_B/f.u. for $H \parallel ab$ and $H \parallel c$, respectively (see SF. 2). At $T = 2$ K, the saturation magnetic moments are $M_S = 3.8$ and 3.2 μ_B/f.u. for $H \parallel ab$ and $H \parallel c$, respectively, obtained from the extrapolation of M versus H^{-1} curves. The value of M_S is 3.2 μ_B/f.u., along $H \parallel c$, which is close to 3.26 μ_B/f.u. found by Clatterbuck and Gschneidner [44]. The observed saturation magnetic moment values are significantly lower than the saturation moment of Ho^{3+} ion, which is expected for the ferrimagnetic arrangement of Mn and Ho atoms. The calculated magnetization of the ferrimagnetic configuration is 3.07 μ_B/f.u. in DFT + U, agreeing reasonably well with experiments. The $M(H)$ measured along $H \parallel c$ at $T = 2$ K shows a square-shaped hysteresis loop with a coercivity of 0.18 T, while the $M(H)$ measured with in-plane fields is nonhysteretic. The hysteretic behaviors for two field directions reverse above T_{SR}, suggesting the change of the easy-cone anisotropy at $T < T_{SR}$ to the easy-plane anisotropy at $T > T_{SR}$.

The magnetic properties of $HoMn_6Sn_6$ were further studied under applied pressure using a Cu-Be mechanical cell with an inner diameter of 2.6 mm, and the lead was used as an internal manometer. The measurements were carried out on the same piece of the sample that has been used for magnetization measurement at ambient pressure (Fig. 2). The pressure calibration from the manometer is presented in SF. 3 [38]. Figure 3 shows magnetization as a function of temperature and magnetic field at pressure up to 0.66 GPa. The SR transition is more pronounced with a peak around 190 K, and the ferrimagnetic-to-paramagnetic transition of Mn sublattice is much more sensitive with pressure. The transition temperature shift from 373 K at ambient pressure [Fig. 2(b)] to 394 K at $P = 0.34$ GPa with $H = 0.1$ T [Fig. 3(a)] and the transition is not complete until 395 K for $P > 0.34$ GPa. The inset of Fig. 3(a) indicates the magnified view of $M(T)$ near $T_C = 376$ K, which clearly shows the shift of T_C for various applied pressure. As shown in the figure, it seems that the critical transition temperature is much higher than 400 K at $P > 0.34$ GPa; however, we do not observe that within our measurement range of 400 K. Considering the value of shift of T_C at P = 0.34 GPa, the T_C shifts to a higher temperature at 53 K/GPa; however, T_C does not necessarily increase linearly with the pressure; therefore a detailed $M(T)$ study at pressure and $T > 400$ K is required.

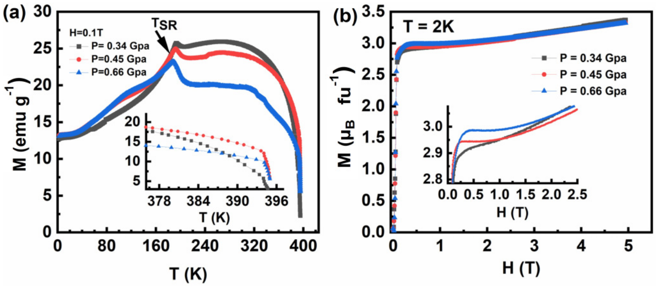

FIG. 3. Pressure-induced magnetization measurements of $HoMn_6Sn_6$ single crystal measured along the $H \parallel c$. (a) Magnetization as a function of temperature, $M(T)$, measured at various hydrostatic pressure at $H = 0.1$ T. The inset indicates the magnified view of $M(T)$ near $T_C = 376$ K. (b) Magnetization as a function of magnetic field at various hydrostatic pressure at $T = 2$ K.

Figure 3(b) presents the isothermal magnetization at various hydrostatic pressure at $T = 2$ K and the inset of Fig. 3(b) shows the pressure dependence of magnetization at low magnetic fields. The magnetic moment at H = 5 T for both above and below the T_{SR} remains relatively the same with $P \geqslant 0.34$ GPa [Fig. 3(b), and SF. 3(d)]. In addition, the saturation moment with pressure is slightly higher compared with the moment at ambient pressure (Fig. 2). For example, the moment at T = 220 K and H = 8 T increases from 5.85 μ_B/f.u. at ambient pressure to 6.6 μ_B/f.u. at $P = 0.66$ GPa. The T_C also increases with pressure, which suggests that interaction between Ho and Mn atoms is enhanced with pressure.

Even if we could not check to get direct experimental evidence, the hydrostatic pressure can likely compress the lattice anisotropically and result in a lowering of the interlayer and interatomic distances between Ho atoms on the 001 plane [Wyckoff site 1a, in (0, 0, 0)] and Mn atoms on planes 004 [in site 6i (1/2, 0, ∼1/4)], which may help to enhance the saturation moment. One may also argue that the pressure introduces anisotropic lattice change, which changes the crystal field and the easy direction of Ho. A decrease of easy-direction angle from 49° could give a larger z-component magnetization and, therefore, an enhancement of moment.

C. Electronic structure of $HoMn_6Sn_6$

Figure 4 presents the electronic structure of $HoMn_6Sn_6$ measured by ARPES and first-principles calculations. We

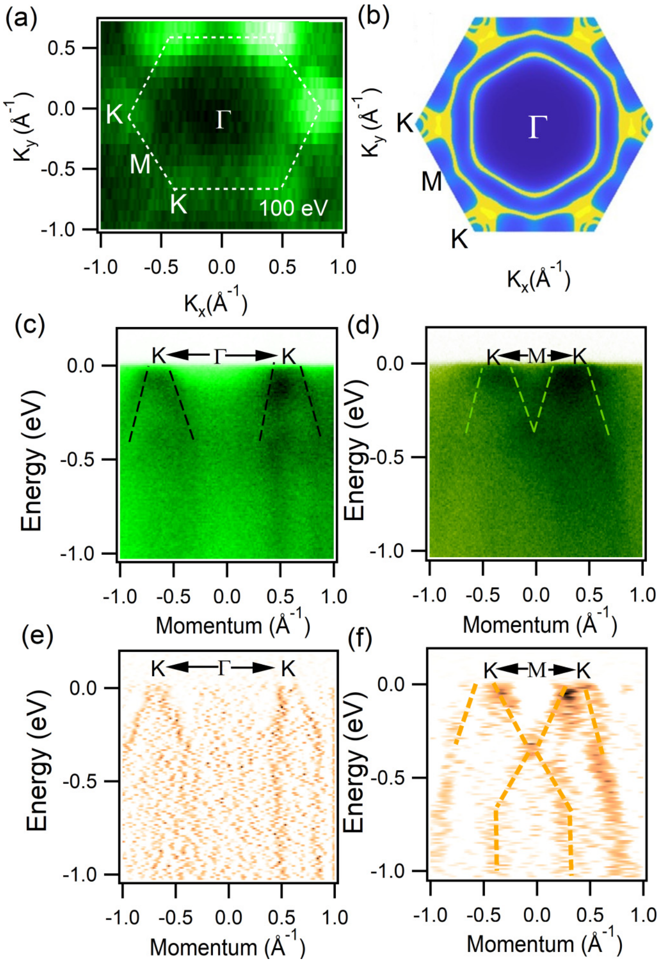

FIG. 4. Fermi surface and dispersion maps of $HoMn_6Sn_6$. (a) Experimentally measured Fermi surface map. (b) Corresponding calculated Fermi surface map. ARPES measured dispersion maps along the (c) K-Γ-K and (d) the K-M-K directions. Second derivative plots along (e) the K-Γ-K and (f) the K-M-K directions.

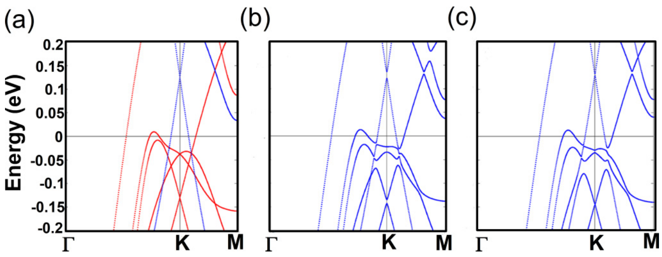

FIG. 5. Band structures of $HoMn_6Sn_6$ along the $\Gamma - K - M$ path near E_F calculated without and with SOC. The bands are calculated at $k_z = 0.25$ r.l.u. (a) Scalar relativistic bands calculated without SOC. Blue and red lines denote two spin channels. (b, c) SOC bands calculated with the spin-quantization direction along the (b) [001] and (c) [100] directions, respectively.

show the Fermi surface (FS) map measured at a temperature of 20 K. The FS map shows the hexagonal symmetry as suggested by the crystal structure. Furthermore, the FS map exhibits the metallic nature, which is accordant with the transport measurements. Six small circles are observed at the BZ corners K, which display a good hexagonal shape (white dotted hexagon). These intense circles at the high-symmetry points K possibly denote multiple bulk bands and the complex band structure of this material. However, all features are not visible in the photoemission intensity plots presented in Fig. 4(a). Figure 4(b) shows the calculated FS, which is a very good match with Fig. 4(a) and reveals the hexagonal shape of the FS map as well.

Next, we discuss the dispersion maps along the high-symmetry directions. Figure 4(c) presents the dispersion map in which linear Dirac-like dispersive bands exist along the K-Γ-K path. The second derivative plot of Fig. 4(c) shows the clean Dirac-like dispersion map crossing the Fermi level [Fig. 4(e)]. Figure 4(d) presents the dispersion map along the K-M-K direction, where electron-like bands exist close to the Fermi level. The corresponding second derivative plot of Fig. 4(d) along the K-M-K direction shows some additional bands at M high-symmetry point [Fig. 4(f)], where the saddle point of the kagome magnet might exist. Dispersion maps along the K-Γ-K direction at various photon energies are presented in Supplemental Fig. 4 (SF. 4). Besides, the dispersion map and corresponding momentum distribution curve (MDC) and energy distribution curve (EDC) along the K-Γ-K path are shown in Supplemental Fig. 5 (SF. 5) [38]. Although $HoMn_6Sn_6$ has been suggested to be a Chern magnet [15], the possible Chern gap above the Fermi level could not be accessed via our ARPES measurement; therefore further study is required to support this claim.

Finally, we discuss the Dirac crossings and SOC-induced gaps and their dependence on the spin orientations. Figure 5 shows the band structures along the Γ-K-M path at $k_z = 0.25$ r.l.u. calculated with and without SOC. This particular k_z value is chosen, according to the photon energy used in ARPES, to better compare with experiments. As shown in Fig. 5(a), multiple Dirac-like crossings occur near E_F at the BZ corners K. Depending on their band characters, different crossings have different k_z dependence. For example, the crossing at $\sim$0.12 eV below E_F is much less k_z dependent than the one right above E_F, showing a more $2D$-like band character.

Figure 5(b) shows the SOC band structures calculated with the spin-quantization direction along the out-of-plane direction. As expected, SOC lifts the orbital degeneracy and splits all crossings at K with various gap sizes. The gaps' sizes depend on the orbital characters of corresponding bands and the SOC Hamiltonian H_{SO}; the latter depends on the spin direction. Figure 5(c) shows the SOC band structures calculated with the spin-quantization axis lying in the basal plane. The SOC-induced gaps become negligibly small or eliminated in comparison with Fig. 5(b), showing the possibility to control the SOC gap size by changing the spin direction. Here we have shown two extreme cases to illustrate the gap evolution with angle change. Note that, in low temperature, the experimental magnetic ordering direction of $HoMn_6Sn_6$ is tilted to 49° with respect to [001], resulting in SOC-induced gap sizes in between the two cases shown in Figs. 5(b) and 5(c) [45]. Since $HoMn_6Sn_6$ undergoes an SR transition with increasing temperature, the SOC-induced gap should also evolve with temperature.

IV. CONCLUSIONS

In summary, we have performed systematic transport, magnetic, and spectroscopic measurements in wide temperature, magnetic-field, and pressure ranges of $\mathrm{HoMn_6Sn_6}$ single crystals. The experimental studies have been supported by first-principles theoretical calculations. Our transport measurement confirms the metallic nature of this compound and shows the signature of a large AHE and contribution of the topological Hall effect in this system. From magnetic measurements, we observe a large hysteresis loop and SR transition below 200 K. We unveil the impact of pressure on magnetic ordering and SR temperature. Our ARPES measurements reveal the presence of Dirac-like states enclosing the high-symmetry point K, supported by the DFT calculations, and suggest the possible existence of a Chern-gapped Dirac-like state in this kagome magnet. Altogether, our detailed studies of the kagome magnet, $\mathrm{HoMn_6Sn_6}$, will provide an ideal platform to understand the magnetotransport properties and the electronic structure of various kagome magnets.

ACKNOWLEDGMENTS

This work was conceived at SUNY Buffalo State and supported by the faculty startup fund from the Dean's Office, School of Arts and Sciences, and Undergraduate Research Office, the State University of New York (SUNY), Buffalo State. R.F. and J.C. acknowledge financial support from Office of Undergraduate Research, EURO, and Small Grant awards. M.N. is supported by the Center for Thermal Energy Transport under Irradiation, an Energy Frontier Research Center funded by the U.S. DOE, Office of Basic Energy Sciences; the Air Force Office of Scientific Research under Award No. FA9550-17-1-0415; and the Air Force Office of Scientific Research MURI (FA9550-20-1-0322). Y.L. and L.K. were supported by the U.S. Department of Energy, Office of Science, Office of Basic Energy Sciences, Materials Sciences and Engineering Division. Ames Laboratory is operated for the U.S. Department of Energy by Iowa State University under Contract No. DE-AC02-07CH11358. N.P. and K.G. acknowledge support from the INL Laboratory Directed Research & Development (LDRD) Program under DOE Idaho Operations Office Contract DE-AC07-05ID14517. We appreciate the support of Nicholas Clark Plumb, Ming Shi, Hang Li and Sailong Ju for the beamline assistance at PSI, SLS.

---

[1] J.-X. Yin, S. S. Zhang, G. Chang, Q. Wang, S. S. Tsirkin, Z. Guguchia, B. Lian, H. Zhou, K. Jiang, I. Belopolski, N. Shumiya, D. Multer, M. Litskevich, T. A. Cochran, H. Lin, Z. Wang, T. Neupert, S. Jia, H. Lei, and M. Z. Hasan, Nat. Phys. **15**, 443 (2019).
[2] T.-H. Han, J. S. Helton, S. Chu, D. G. Nocera, J. A. Rodriguez-Rivera, C. Broholm, and Y. S. Lee, Nature (London) **492**, 406 (2012).
[3] I. I. Mazin, H. O. Jeschke, F. Lechermann, H. Lee, M. Fink, R. Thomale, and R. Valenti, Nat. Commun. **5**, 4261 (2014).
[4] Z. Guguchia, J. A. T. Verezhak, D. J. Gawryluk, S. S. Tsirkin, J.-X. Yin, I. Belopolski, H. Zhou, G. Simutis, S.-S. Zhang, T. A. Cochran, G. Chang, E. Pomjakushina, L. Keller, Z. Skrzeczkowska, Q. Wang, H. C. Lei, R. Khasanov, A. Amato, S. Jia, T. Neupert *et al.*, Nat. Commun. **11**, 559 (2020).
[5] J. Wang and S.-C. Zhang, Nat. Mater. **16**, 1062 (2017).
[6] M. Z. Hasan and C. L. Kane, Rev. Mod. Phys. **82**, 3045 (2010).
[7] J.-X. Yin, W. Ma, T A Cochran, X. Xu, S. S. Zhang, H.-J. Tien, N. Shumiya, G. Cheng, K. Jiang, B. Lian, Z. Song, G. Chang, I. Belopolski, D. Multer, M. Litskevich, Z.-J. Cheng, X. P. Yang, B. Swidler, H. Zhou, H. Lin, T. Neupert *et al.*, Nature (London) **583**, 533 (2020).
[8] X. G. Wen, Rev. Mod. Phys. **89**, 041004 (2017).
[9] J.-X. Yin, S. S. Zhang, H. Li, K. Jiang, G. Chang, B. Zhang, B. Lian, C. Xiang, I. Belopolski, H. Zheng, T. A. Cochran, S.-Y. Xu, G. Bian, K. Liu, T.-R. Chang, H. Lin, Z.-Y. Lu, Z. Wang, S. Jia, W. Wang *et al.*, Nature (London) **562**, 91 (2018).
[10] L. Ye, M. Kang, J. Liu, F. V. Cube, C. R. Wicker, T. Suzuki, C. Jozwiak, A. Bostwick, E. Rotenberg, D. C. Bell, L. Fu, R. Comin, and J. G. Checkelsky, Nature (London) **555**, 638 (2018).
[11] S. Yan, D. A. Huse, and S. R. White, Science **332**, 1173 (2011).
[12] E. Liu, Y. Sun, N. Kumar, L. Muechler, A. Sun, L. Jiao, S.-Y. Yang, D. Liu, A. Liang, Q. Xu, J. Kroder, H. Borrmann, C. Shekhar, Z. Wang, C. Xi, W. Wang, W. Schnelle, S. Wirth, Y. Chen, S. T. B. Goennenwein *et al.*, Nat. Phys. **14**, 1125 (2018).
[13] L. A. Fenner, A. A. Dee, and A. S. Wills, J. Phys.: Condens. Matter **21**, 452202 (2009).
[14] S. Nakatsuji, N. Kiyohara, and T. Higo, Nature (London) **527**, 212 (2015).
[15] W. Ma, X. Xu, J.-X. Yin, H. Yang, H. Zhou, Z.-J. Cheng, Y. Huang, Z. Qu, F. Wang, M. Z. Hasan, and S. Jia, Phys. Rev. Lett. **126**, 246602 (2021).
[16] A. K. Nayak, J. E. Fischer, Y. Sun, B. Yan, J. Karel, A. C. Komarek1, C. Shekhar1, N. Kumar1, W. Schnelle1, J. Kubler, C. Felser1, and S. S. P. Parkin, Sci. Adv. **2**, e1501870 (2016).
[17] E. Tang, J.-W. Mei, and X.-G. Wen, Phys. Rev. Lett. **106**, 236802 (2011).
[18] G. Xu, B. Lian, and S.-C. Zhang, Phys. Rev. Lett. **115**, 186802 (2015).
[19] G. Venturini, R. Welter, B. Malaman, and E. Ressouche, J. Alloys Compd. **200**, 51 (1993).
[20] J. Hu, K.-Y. Wang, B.-P. Hu, Y.-Z. Wang, Z. Wang, F. Yang, N. Tang, R. Zhao, and W. Qin, J. Phys.: Condens. Matter **7**, 889 (1995).
[21] J. Hu, F. Yang, Y. Wang, J. Wang, and F. R. de Boer, Phys. Stat. Sol. (b) **214**, 135 (1999).
[22] N. K Zajkov, N. V. Mushnikova, M. I. Bartashevich, and T. Goto, J. Alloys Compd. **309**, 26 (2000).
[23] J.-L. Yao, S. Zhang, B. Liu, and B. Shen, J. Appl. Phys. **95**, 7061 (2004).
[24] Sh. Tabatabai Yazdi, N. Tajabor, M. R. Roknabadi, M. Behdani, and F. Pourarian, J. Magn. Magn. Mater. **324**, 723 (2012).
[25] T. Asaba, S. M. Thomas, M. Curtis, J. D. Thompson, E. D. Bauer, and F. Ronning, Phys. Rev. B **101**, 174415 (2020).

[26] N. J. Ghimire, R. L. Dally, L. Poudel, D. C. Jones, D. Michel, N. T. Magar, M. Bleuel, M. A. McGuire, J. S. Jiang, J. F. Mitchell, J. W. Lynn, and I. I. Mazin, Sci. Adv. **6**, eabe2680 (2020).

[27] H. Zhang, X. Feng, T. Heitmann, A. I. Kolesnikov, M. B. Stone, Y.-M. Lu, and X. Ke, Phys. Rev. B **101**, 100405(R) (2020).

[28] Q. Wang, K. J. Neubauer, C. Duan, Q. Yin, S. Fujitsu, H. Hosono, F. Ye, R. Zhang, S. Chi, K. Krycka, H. Lei, and P. Dai, Phys. Rev. B **103**, 014416 (2021).

[29] L. Gao, S. Shen, Q. Wang, W. Shi, Y. Zhao, C. Li, W. Cao, C. Pei, J.-Y. Ge, G. Li, J. Li, Y. Chen, S. Yan, and Y. Qi, Appl. Phys. Lett. **119**, 092405 (2021).

[30] G. Dhakal, F. Cheenicode Kabeer, A. K. Pathak, F. Kabir, N. Poudel, R. Filippone, J. Casey, A. P. Sakhya, S. Regmi, C. Sims, K. Dimitri, P. Manfrinetti, K. Gofryk, P. M. Oppeneer, and M. Neupane, Phys. Rev. B **104**, L161115 (2021).

[31] G. Venturini, B. Chafik ElIdrissi, and B. Malaman, J. Magn. Magn. Mater. **94**, 35 (1991).

[32] G.-H. Guo, J. Qin, and H.-B. Zhang, J. Alloys Compd. **429**, 46 (2007).

[33] B. C. El Idrissi, G. Venturini, and B. Malaman, J. Less-Common Met. **175**, 143 (1991).

[34] C. Lefevre and G. Venturini, J. Magn. Magn. Mater. **268**, 374 (2004).

[35] D. J. Thouless, M. Kohmoto, M. P. Nightingale, and M. den Nijs, Phys. Rev. Lett. **49**, 405 (1982).

[36] F. D. M. Haldane, Phys. Rev. Lett. **61**, 2015 (1988).

[37] J. Zou, Z. He, and G. Xu, npj Comput. Mater. **5**, 96 (2019).

[38] See Supplemental Material at http://link.aps.org/supplemental/10.1103/PhysRevMaterials.6.064404 for crystal growth and energy dispersive X-ray spectroscopy of $\mathrm{HoMn_6Sn_6}$, isothermal magnetization curves at temperatures 20 to 390 K, pressure determination for magnetic measurements, dispersion map, and corresponding MDC and EDC along the K-Γ-K direction.

[39] P. Blaha, K. Schwarz, F. Tran, R. Laskowski, G. K. H. Madsen, and L. D. Marks, J. Chem. Phys. **152**, 074101 (2020).

[40] J. P. Perdew, K. Burke, and M. Ernzerhof, Phys. Rev. Lett. **77**, 3865 (1996).

[41] G. Pizzi, V. Vitale, R. Arita, S. Blugel, F. Freimuth, G. Geranton, and M. Gibertini, J. Phys.: Condens. Matter **32**, 165902 (2020).

[42] B. Malaman, G. Venturini, R. Welter, J. Sanchez, P. Vulliet, and E. Ressouche, J. Magn. Magn. Mater. **202**, 519 (1999).

[43] H. Li, B. Ding, J. Chen, Z. Li, E. Liu, X. Xi, G. Wu, and W. Wang, Appl. Phys. Lett. **116**, 182405 (2020).

[44] D. M Clatterbuck and K. A. Gschneidner Jr., J. Magn. Magn. Mater. **207**, 78 (1999).

[45] Y. Lee, R. Skomski, X. Wang, P. P. Orth, A. K. Pathak, B. N. Harmon, R. J. McQueeney, I. I. Mazin, and L. Ke, arXiv:2201.11265.